ROYAL SOCIETY
OF CHEMISTRY

PAPER

Check for updates

Boosting sodium-ion mobility in $Na_3V_2(PO_4)_2F_3$ through anion engineering with Br^- substitution

Sankalpita Chakrabarty,[ab] Ziliang Wang,[cd] Arun Krishnan,[ab] Arad Paperni,[ab] Sarah Taragin,[ab] Reut Yemini,[ab] Ilana Perelshtein,[b] Ayan Mukherjee [ID] *[ab] and Malachi Noked [ID] *[ab]

Enhancing Na-ion intercalation in $Na_3V_2(PO_4)_2F_3$ (NVPF) without compromising cycling stability is crucial for the development of high-performance sodium-ion batteries. This study demonstrates that partial substitution of F^- with less electronegative Br^- in NVPF facilitates electrochemical activation of the third Na ion while preserving structural integrity. A series of Br-substituted NVPF hollow microspheres, $Na_3V_2(PO_4)_2F_{3(1-x)}Br_{3x}$ (x = 0.1, 0.2, 0.3, 0.4), were synthesized and evaluated. Among them, NVPF-Br (x = 0.2) exhibited the highest electrochemical performance, delivering a high discharge capacity of 169 mA h g^{-1} at 64 mA g^{-1} within a 1.2–4.3 V window and retaining 134 mA h g^{-1} with 100% coulombic efficiency after 150 cycles. Structural analysis revealed that optimised Br substitution causes the structural transformation from orthorhombic to tetragonal structure. This structural rearrangement expands the 2D tunnel framework, enabling faster Na-ion diffusion and reducing migration activation energy, as confirmed by density functional theory (DFT) and nudged elastic band (NEB) calculation. Moreover, a stable cathode electrolyte interphase (CEI) layer, minimal irreversible capacity loss, and suppressed carbonate formation contributed to improved long-term cycling stability. These findings demonstrate the role of Br substitution in optimizing NVPF cathodes for next-generation sodium-ion batteries.

Introduction

Over the past few decades, lithium-ion batteries (LIB) have been integrated into our daily lives, driven by the steadily increasing global energy demands.[1–6] More recently, the success of LIBs has extended to sodium-ion batteries (SIBs), owing to the high natural abundance of sodium, lower cost, and a similar intercalation mechanism to that of Li.[5,7–10] However, SIB technology still faces significant challenges, including lower energy density compared to LIBs and a limited selection of suitable electrode materials, which must be addressed to enable broader adoption. Current SIB systems are mostly based on carbon anodes and either Na-based layered oxides or various polyanionic materials as cathodes.[11–17] The layered oxides materials recently have drawn considerable interest due to their high theoretical capacity. Layered oxides are classified as P2, P3, or O3, where "P" and "O" denote prismatic or octahedral Na^+ coordination, and the number indicates the oxygen-layer stacking sequence.

Their structural framework contains two-dimensional alkali ion diffusion channels, which reduces the Na ion diffusion barrier, compared to denser crystal structure, enabling high capacity. However, despite better kinetics, the intermediate phase transition (P2 ↔ O2, O3 ↔ P3) during cycling leads to rapid capacity fading, which is a major disadvantage of layered oxide sodium cathodes. On another note, the layered oxides suffer limited air/moisture stability which hinders their overall efficiency in practical application. In this perspective the phosphate based polyanionic materials show their framework stability at ambient atmosphere which is a major advantage in production level technology.[18,19] Among the polyanionic materials, $Na_3V_2(PO_4)_2F_3$ (NVPF) is a particularly promising candidate, offering reversible extraction of two Na ions per formula unit through two main voltage plateaus centered at ~3.7 V and ~4.2 V *vs.* Na/Na^+, with a theoretical reversible capacity of 128 mA h g^{-1}. Moreover, its excellent capacity retention and rate capability make NVPF a reliable positive electrode material for SIBs.[20–22]

Despite these benefits, the specific energy of NVPF-based SIBs must be further improved to compete with Li electrodes (600 W h kg^{-1} for $LiCoO_2$ material). Therefore, considerable research in recent years has focused on increasing the capacity of NVPF electrodes. The concept of inserting more Na ions into the $Na_3V_2(PO_4)F_3$ structure was first described by Zhang *et al.*,

aDepartment of Chemistry, Bar Ilan University, Ramat Gan, Israel. E-mail: Malachi. Noked@biu.ac.il

bBar-Ilan Institute of Nanotechnology and Advanced Materials, Ramat Gan, Israel

cDepartment of Materials Science and Engineering, National University of Singapore, 9 Engineering Drive 1, 117575, Singapore

dDepartment of Materials Science and Engineering, Northwestern University, Evanston, Illinois, 60208, USA

who employed a ball-milling process to enhance capacity successfully. Their study focused on the 1st and 2nd cycles and demonstrated cycling stability up to 20 cycles.[23] An additional electrochemical approach was introduced by Bianchini et al., towards the insertion/extraction of a 3rd Na-ion within a wide potential window of 1.0–4.5 (vs. Na/Na$^+$), which provides an additional capacity of 65 mA h g^{-1} for $Na_3V_2(PO_4)_2FO_2$.[24] Interestingly, no significant capacity improvement is noticed for $Na_3V_2(PO_4)F_3$ even at low potential (below 2.0 V vs. Na/Na$^+$) due to the large Na migration barrier. The study mostly focused on the doping of the redox active cation to improve Na insertion potential. Despite their important achievement in refining energy density, cycling stability is still under consideration. Another pathway to improve the energy density involves utilizing the remaining Na, which could yield an energy density of ~800 W h kg^{-1} (based on active material) at higher potentials (>4.9 V).[25,26] Nevertheless, such high voltage is not compatible with current Na electrolyte systems due to limited anodic stability.

Recently, Canepa et al. proposed a theoretical strategy to improve the energy density of pristine NVPF by ~14% through transition metal mixing. This approach enables the extraction of the 3rd Na-ion by activating alternative redox couples to high-potential V$^{4+/5+}$.[27] Furthermore, Yan et al. achieved the extraction of nearly three Na ions via electrochemical charging up to 4.8 V (vs. Na/Na$^+$), resulting in a sodium-driven charge compensation mechanism involving vanadium oxidation states ranging from +3 to +4.5. This process led to a disordered NVPF structure that remained stable over 25 cycles. According to their study, the NVPF structure underwent a phase transformation from orthorhombic to tetragonal.[28] This phase transformation occurs at high potential only when more than 2.5Na ion is extracted. Upon sodiation, the original phase is not recovered, and instead, a disordered configuration emerges, suggesting partial irreversibility in the structural dynamics. Even though this is an exclusive and efficient approach to integrate the 3rd Na ion in redox activity, the structural stability is yet to be conclusively determined upon cycling.

In our previous study, we demonstrated the controlled synthesis of NVPF with a hollow microstructure, which offers high specific capacity (197 mA h g^{-1}) over a wide potential range from 1 V to 4.8 V (vs. Na/Na$^+$). However, maintaining structural stability over prolonged cycling remains a major challenge within this extended potential window.[20] The experimental extraction of the 3rd sodium is particularly difficult due to the stability of the V–O bonding environment and the strong coulombic attraction between Na$^+$ and the surrounding anions.

A notable computational analysis by Xu et al. proposed a potential strategy for modifying the material to enable the extraction of the 3rd Na ion within the stable electrolyte region by swapping the anions O and F with less electronegative elements such as Cl or Br. Compared to F, Br is less electronegative and hence attracts less negative charge, reducing the binding energy to the positively charged Na ions.[29] However, these theoretical predictions have yet to be demonstrated experimentally. Collectively, these studies provide a pathway toward the improvement of Na electrochemistry and have inspired the present study. Hence, in this work, we demonstrate the electrochemical significance of partially replacing F$^-$ with Br$^-$ in the NVPF structure. To serve this purpose, a series of materials were synthesized in which F is partially substituted with varying amounts of Br, forming $Na_3V_2(PO_4)_2F_{3(1-x)}Br_{3x}$ (x = 0.1, 0.2, 0.3, 0.4), each exhibiting a hollow microsphere morphology. The compositions $Na_3V_2(PO_4)_2F_{2.7}Br_{0.3}$, $Na_3V_2(PO_4)_2F_{2.4}Br_{0.6}$, $Na_3V_2(PO_4)_2F_{2.1}Br_{0.9}$, and $Na_3V_2(PO_4)_2F_{1.8}Br_{1.2}$, are hereafter referred to as NVPF-Br (x = 0.1), NVPF-Br (x = 0.2), NVPF-Br (x = 0.3), NVPF-Br (x = 0.4), respectively. Interestingly, the optimal amount of Br (x = 0.2) substitution level leads to a significant enhancement in electrochemical performance when used as a cathode material for SIBs, during extraction and insertion of more than 2Na ions (within the potential range of 1.2 to 4.3 V vs. Na/Na$^+$). Notably, this is the first demonstration of cycling stability over 150 cycles with intercalation/deintercalation of more than 2Na ions at a high current density of 64 mA g^{-1}. Structural refinement reveals a significant increase in the c lattice parameter for NVPF-Br (x = 0.2). This lattice expansion induces a structural transformation from the orthorhombic framework observed in pristine NVPF to a tetragonal phase. Such a rearrangement leads to the widening of the two-dimensional (2D) diffusion tunnels, thereby facilitating enhanced Na$^+$ ion mobility. This structural evolution and its impact on ion transport are further corroborated by density functional theory (DFT) calculations and nudged elastic band (NEB) analysis, which confirm the reduction in migration energy barriers along the expanded tunnels.

Results and discussion

To investigate the effect of Br substitution on the morphology of NVPF, scanning electron microscopy (SEM) was performed on the pristine and Br-substituted samples ($Na_3V_2(PO_4)_2F_{3(1-x)}Br_x$, x = 0.1, 0.2, 0.3, 0.4), as depicted in Fig. 1a–e. All the materials exhibit a well-defined hollow microsphere-like morphology with an average diameter of 1 μm. The inset of Fig. 1a displays that the microsphere surface of NVPF is composed of tiny secondary nanoparticles, which contribute to surface porosity. Upon introducing 10% Br substitution (NVPF-Br, x = 0.1), the surface begins to show noticeable modifications compared to the pristine NVPF. The building block of the hollow microspheres transforms from a tiny nanoparticle to square-shaped units. In NVPF-Br (x = 0.2), the surface becomes more densely packed and smoother, accompanied by an increase in the aperture diameter of the hollow structure. With further increments of NVPF-Br (x = 0.3 and x = 0.4), the square-shaped secondary particles gradually transform into plate-like elements that stack together to form the sphere. The growth process is governed by the oriented aggregation of secondary nanoparticles through Ostwald ripening.[30] The hollow spherical morphology of NVPF-Br (x = 0.2) is further confirmed by the transmission electron microscopy (TEM) image shown in Fig. 1f. The crystalline structure of the material is supported by the high-resolution TEM (HRTEM) pattern, where the measured interplanar spacings correspond to the (220) plane, in good agreement with the NVPF phase (inset Fig. 1f).
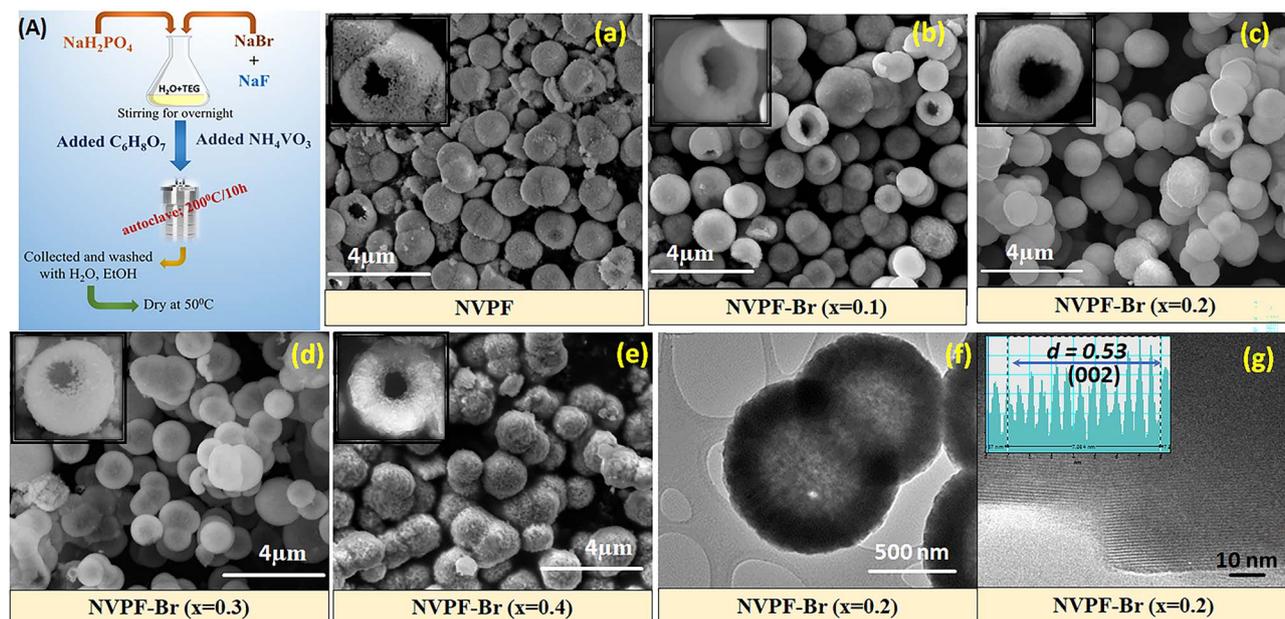
Fig. 1 (A) Schematic illustration of synthesis protocol; SEM images of (a) NVPF, (b) NVPF–Br ($x = 0.1$), (c) NVPF–Br ($x = 0.2$), (d) NVPF–Br ($x = 0.3$), and (e) NVPF–Br ($x = 0.4$) [magnification 20 000×, scale bar indicates 4 μm]; insets show corresponding high-magnification [magnification 120 000×] images. (f) and (g) TEM and HRTEM image of NVPF–Br ($x = 0.2$); inset of (g) shows the 'd' spacing calculated from fringe pattern.

The structural purity of the synthesized materials was examined by X-ray diffraction (XRD), as shown in Fig. 2a. The diffraction patterns match well with the reference pattern (#01-089-8485) and show no evidence of impurity phases.[31] Notably, Br substitution does not create any impurity and/or secondary phases. However, the magnified 2θ zone (inset of Fig. 2a) shows a gradual shift of the diffraction peaks toward lower angles with increasing Br content. This peak shift indicates an expansion of
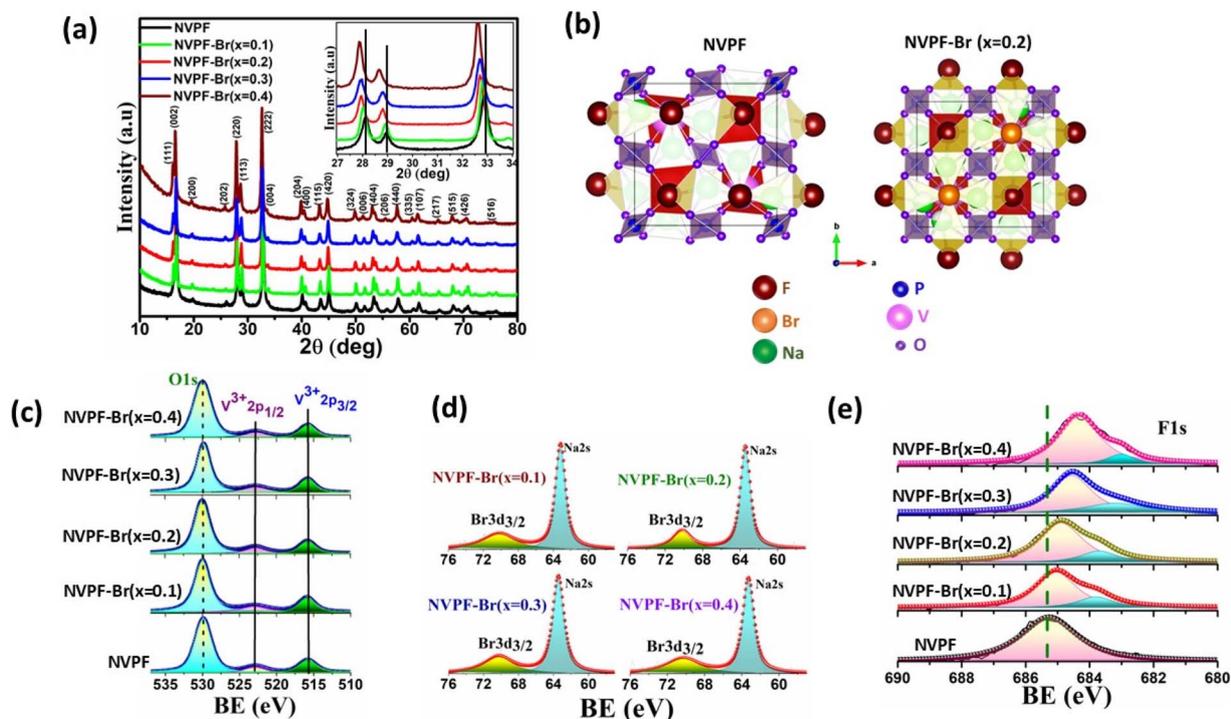

Fig. 2 Structural and surface chemical analysis of NVPF materials. (a) XRD pattern of all synthesized materials; inset shows the magnified 2θ zone. (b) Refined structural representation of atomic arrangement in NVPF and NVPF–Br ($x = 0.2$); XPS spectra of (c) O 1s and V 2p, (d) Br 3d, and (e) F 1s.

33296 | J. Mater. Chem. A, 2025, 13, 33294–33304

This journal is © The Royal Society of Chemistry 2025

interlayer spacings within the crystal structure, which is consistent with the larger ionic radius of Br compared to F. Detailed refinement of structural and microstructural parameters has been described in our previous report.[32]

Based on this analysis, NVPF exhibits an orthorhombic structure with the *Amam* space group. The detailed structural data of pristine NVPF are provided in our earlier publications.[20,31] In NVPF-Br ($x = 0.1$), the orthorhombic distortion with the *Amam* space group is preserved (Table S1). The original framework of NVPF, consisting of $V_2O_8F_3$ bi-octahedral units coupled by a corner-sharing PO_4 tetrahedral unit, is well preserved. The Na ions are located at fully occupied pyramidal sites (Na1), partially occupied pyramidal sites (Na2), and partially occupied capped prismatic sites (Na3) (Fig. 2b). The structure exhibits distortion, as observed by variations in unit cell parameters. Although the a and b parameters do not change significantly, the unit cell parameter c decreases significantly, which implies that the structure is unstable. The structural reordering is led by changes in bond lengths and adjustments in bond angles between the $V_2O_8F_{2.7}Br_{0.3}$ bi-octahedral units and PO_4 tetrahedral units in the b–c plane. This leads to a decrease in the lattice parameter along the b and c direction, and a slight apparent increase along a, as revealed by our structural refinement. This distortion appears from the $V_2O_8F_{2.7}Br_{0.3}$ bi-octahedral units disrupting orthorhombic framework in the a–b plane. In NVPF-Br ($x = 0.2$), the orthorhombic structure is completely converted to a tetragonal structure with the $I4/mmm$ space group, consistent with the structure previously observed by Yan et al.[33]

This structural transformation arises due to significant variation in the unit cell parameter c, due to the stronger electrostatic repulsion, which is no longer screened by the Na ions. The detailed lattice parameters obtained from Rietveld refinement are presented in Table S2. The structure, containing a large 2D tunnel and $V_2O_8F_{2.4}Br_{0.6}$ bi-octahedral units coupled by a corner-sharing PO_4 tetrahedral unit, remains well preserved. The 3D framework shows greater stability in NVPF-Br ($x = 0.2$). In NVPF-Br ($x = 0.2$), the unit cell volume increases significantly due to the increase in the c lattice parameter. The bond lengths between the $V_2O_8F_{2.4}Br_{0.6}$ bi-octahedral unit and the PO_4 tetrahedral unit change only slightly (V–F1 bond increases from 1.96 Å to 2.03 Å in V–Br1, and the V–F2 bond increases from 1.94 Å to 1.99 Å in V–Br2). The V–F1–V bond angle in NVPF (179.9°) decreases to 172.7° in V–Br1–V within the b–c plane of the $V_2O_8F_{2.4}Br_{0.6}$ bi-octahedra (Fig. 2b).

The structural rearrangement observed in NVPF-Br ($x = 0.2$) increases the width of the 2D tunnel structure and facilitates Na ion migration. In NVPF-Br ($x = 0.3$), the same crystal structure as in NVPF-Br ($x = 0.2$) is preserved, although the unit cell parameters and overall volume decrease. This reduction is attributed to the increase in the micro-strain induced during Br substitution. The detailed structural and microstructural parameters are listed in Table S3. In contrast, NVPF-Br ($x = 0.4$) exhibits a different tetragonal symmetry, assigned to the $P4_2nm$ space group (Table S4). The large micro-strain generated at this composition leads to lattice contraction and decreases the unit cell volume, as detailed in Table S5.

Inductively coupled plasma atomic emission spectroscopy (ICP-AES) was conducted to confirm the stoichiometry of Na and V in the samples. A consistent Na : V ratio of ~1.5 was observed for all the samples, aligning well with their intended synthesis. The measured molar densities of Br were 7 mM g^{-1}, 14.1 mM g^{-1}, 20.89 mM g^{-1} and 28.6 mM g^{-1} for NVPF-Br ($x = 0.1$), NVPF-Br ($x = 0.2$), NVPF-Br ($x = 0.3$) and NVPF-Br ($x = 0.4$), respectively. Correspondingly, the F : Br ratios were found to be 8.96 : 1, 4.12 : 1, 2.34 : 1, and 1.54 : 1 for the same compositions. Although ICP-AES only provides elemental concentration without details on dopant distribution within the structure, it confirms the stoichiometry of Br in our synthesized material.

Further XPS analysis was conducted to determine the oxidation state of vanadium ions in both pristine NVPF and Br-substituted NVPF materials, as shown in Fig. 2c. The XPS fine spectra of O 1s at 530.0 eV were used to extract the positions of V $2p_{3/2}$ and V $2p_{1/2}$ peaks at 515.8 eV and 522.8 eV, respectively, for all synthesized materials. These values indicate the +3 oxidation state of vanadium.[32] Notably, no shift in the V 2p binding energies is observed with increasing Br content, indicating that the oxidation state of vanadium remains stable upon Br substitution. The presence of Br is further confirmed by the Br 3d spectra (Fig. 2d), which displays a peak at 70.5 eV. The Br $3d_{3/2}$ binding energy remains unchanged across different Br concentrations.[34] However, the substitution of F influences the F 1s spectra, presented in Fig. 2e. Increasing Br content subsequently causes a reduction in the F content, and a gradual shift of the F 1s spectra to lower binding energies is detected from the XPS study. For samples with higher F content, the peak appears symmetric and consists of a single component. However, as the F content decreases, an additional smaller peak emerges at lower binding energy. This secondary peak is likely attributed to the abatement of local surface-bound F and increased exposure of the inner surface, where the adsorbed F 1s component contributes to the asymmetric nature. Even though XPS is limited to surface sensitivity, this experimental observation of the spectral changes indicates the change in F content due to Br substitution. The Br peaks also suggest that the bromine species are not precipitated but rather incorporated into the host NVPF. Nevertheless, in this work we are not showing direct evidence for bulk substitution of Br, and it belongs in our next studies.

The initial charge–discharge profiles, measured within the potential window of 4.3 V to 1.2 V *vs.* Na/Na$^+$ (Fig. 3a), reveal that NVPF-Br ($x = 0.2$) exhibits the lowest irreversible capacity loss, at 21.2 mA h g^{-1}, compared to pristine NVPF (49.68 mA h g^{-1}), NVPF-Br ($x = 0.1$) (72.39 mA h g^{-1}), NVPF-Br ($x = 0.3$) (43.61 mA h g^{-1}), and NVPF-Br ($x = 0.4$) (51.74 mA h g^{-1}). Further, it is observed that NVPF-Br ($x = 0.2$) exhibits initial charge/discharge capacities of 149.2 and 128 mA h g^{-1}, corresponding to the extraction of 2.33Na$^+$ ions and reinsertion of 2Na$^+$ ions. The 1st cycle capacity loss for NVPF-Br ($x = 0.2$) is 14.2%, significantly lower than the 26% loss observed for pristine NVPF. The poorest performance is seen in NVPF-Br ($x = 0.1$), which shows the lowest discharge capacity (~91 mA h g^{-1}) and the highest initial capacity loss (~44%). NVPF-Br ($x = 0.3$) and NVPF-Br ($x = 0.4$) exhibit capacity losses of 25.8% and 30%,

This journal is © The Royal Society of Chemistry 2025

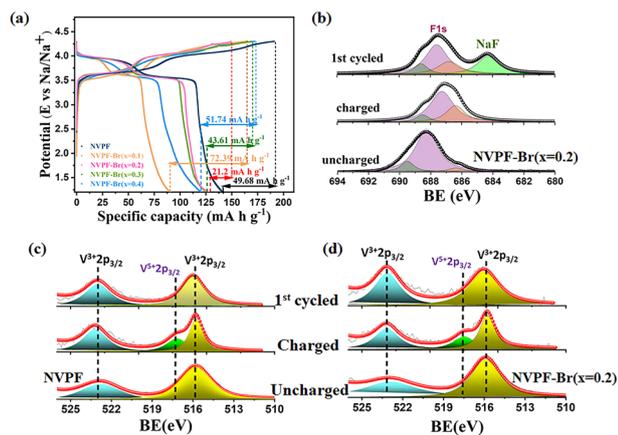*J. Mater. Chem. A*, 2025, **13**, 33294–33304 | **33297**

Fig. 3 Electrochemical performance and surface chemical states of NVPF and Br-substituted materials. (a) 1st cycle charge–discharge profiles of all synthesized materials at C/15 rate. (b) F 1s XPS spectra of uncharged NVPF-Br ($x = 0.2$), after the 1st charge, and after the 1st cycle. V 2p XPS spectra, uncharged, after 1st charged and 1st cycle, of (c) pristine NVPF and (d) NVPF-Br ($x = 0.2$).

respectively, with corresponding discharge capacities of 125.3 mA h g^{-1} and 120.3 mA h g^{-1}. A comparative summary of these results is provided in Table 1.

The XPS fine spectra of F 1s and V 2p for the uncharged, charged, and 1st cycled cathode are presented in Fig. 3b–d. In the uncharged state, the F 1s spectrum of the electrode, containing PVDF (Polyvinylidene Fluoride) binder and carbon black, shows an overall shift to higher binding energies compared to the powder material. This shift is associated with the presence of C–F, PVDF, and P–F bonds in the 686–689 eV range, a well-documented phenomenon in the literature.[34–38] In the charged state, the F 1s spectrum of the NVPF-Br ($x = 0.2$) electrode shows a small shift to lower binding energy. In contrast, a minor trace of NaF formation, located at 684 eV, is observed in the NVPF electrode. After the 1st cycle, the NaF peak becomes the most intense in the NVPF-Br ($x = 0.2$) electrode compared to the other synthesized materials (Fig. S2), whereas the NVPF-Br ($x = 0.4$) sample exhibits the weakest intensity. The formation of NaF after the 1st cycle is directly related to the development of cathode electrolyte interphase (CEI). Generated through the decomposition of the electrolyte (NaPF$_6$ in PC + 2% FEC) on the cathode surface. The oxidative decomposition of PF^{6-} ion initiates a series of reactions with both the electrolyte solvent and the electrode surface resulting in the formation of

inorganic compound of the CEI layer, predominantly NaF. At the same time, the decomposition of PC at higher voltage (above 4.0 V *vs.* Na/Na$^+$) leads to generating organic byproducts including polycarbonates, carboxylates, and gaseous CO$_2$. These species are accountable to create unstable and inhomogeneous CEI layer and often associated with increased interfacial impedance. The inclusion of FEC additive mitigates this effect by the suppressing of PC decomposition at higher voltage and concurrently undergoes preferential reduction at cathodic environment which yields NaF. The CEI layer thus formed is enriched in inorganic species, mainly NaF and Na$_2$CO$_3$.[39–41] Interestingly, the presence of NaF in the CEI layer plays a beneficial role by forming a more stable electronic insulation layer, which prevents further electrolyte decomposition and mitigates the side reactions. This observation supports the potential for long-term cycling stability of the NVPF-Br ($x = 0.2$) cathode. Additionally, the V 2p XPS spectra of NVPF-Br ($x = 0.2$) and pristine NVPF were recorded in the charged state and after the 1st cycle as well, as presented in Fig. 3c and d. In the uncharged state, the trivalent oxidation state of vanadium, V 2p$_{3/2}$ peak appears at 515.8 eV. Once charged to 4.3 V *vs.* Na/Na$^+$, this peak splits into a doublet at 515.8 eV and 517.3 eV, corresponding to trivalent and pentavalent oxidation states of vanadium, respectively, observed in both pristine and Br-substituted electrodes.[11,15] The average vanadium oxidation states, obtained from peak broadening for pristine NVPF, NVPF-Br ($x = 0.1$), NVPF-Br ($x = 0.2$), NVPF-Br ($x = 0.3$), and NVPF-Br ($x = 0.4$), are 4.49, 4.27, 4.17, 4.32, and 4.35, respectively, consistent with the extent of Na ions extraction during charging. Upon discharging, the V 2p$_{3/2}$ peak is returned to the singlet curve, confirming the reversion to the +3 oxidation state and indicating stable redox activity of the cathode materials within this potential range. These findings align with the initial galvanostatic profile, which shows that the NVPF-Br ($x = 0.2$) cathode exhibits the lowest irreversible capacity loss (~14%) (Fig. 3a) and a strong signature of NaF in the XPS spectra (Fig. 3b), supporting the formation of a stable CEI layer on the cathode surface.

The rate performance was evaluated at current densities ranging from 8.5 to 384 mA g^{-1}, followed by a reversion to 12.8 mA g^{-1} and cycling at 25.6 mA g^{-1} (Fig. 4a). Pristine NVPF exhibited discharge capacities of 139, 135, 137, 130, 118, 107, and 99 mA h g^{-1} at current densities of 8.5, 12.8, 25.6, 64, 128, 256, and 384 mA g^{-1}, respectively. In comparison, NVPF-Br ($x = 0.2$) demonstrated superior capacity retention, delivering 128, 132, 134, 130, 125, 115, and 108 mA h g^{-1} at the corresponding

Table 1 Initial charge–discharge capacities and capacity loss for pristine and Br-substituted NVPF materials

Material	1st charge capacity (mA h g^{-1})	1st discharge capacity (mA h g^{-1})	Initial capacity loss (mA h g^{-1})	% of capacity loss
NVPF	190.96	141.28	49.68	26
NVPF-Br ($x = 0.1$)	163.29	90.9	72.39	44.3
NVPF-Br ($x = 0.2$)	149.2	128	21.2	14.2
NVPF-Br ($x = 0.3$)	168.9	125.29	43.61	25.8
NVPF-Br ($x = 0.4$)	172.03	120.29	51.74	30

33298 | *J. Mater. Chem. A*, 2025, **13**, 33294–33304

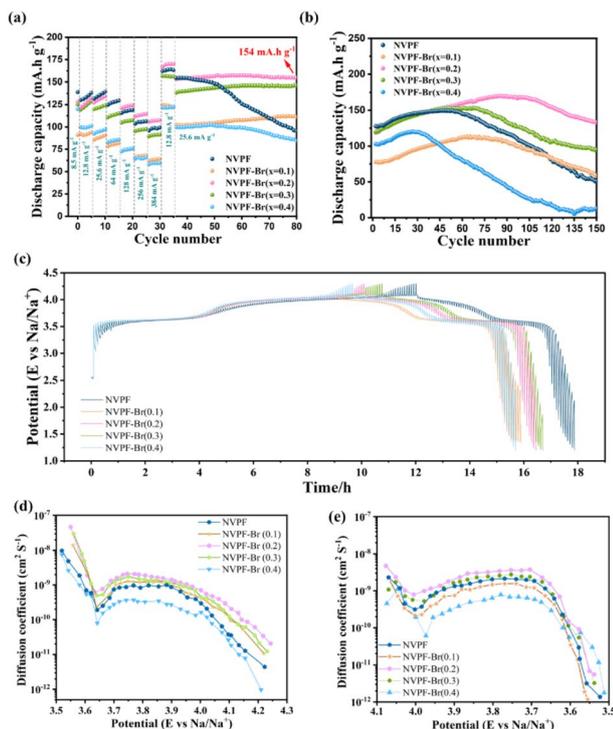This journal is © The Royal Society of Chemistry 2025

Fig. 4 Electrochemical performance and Na$^+$ diffusion behavior of pristine and Br-substituted NVPF cathodes. (a) Rate performance and (b) cycling profile at a current density of 64 mA g^{-1} for all synthesized cathode materials. (c) Galvanostatic intermittent titration technique (GITT) curves; variation of Na$^+$ diffusion coefficient during the (d) charge and (e) discharge process.

current rates. The other Br-substituted compositions showed relatively lower capacities, with NVPF-Br ($x = 0.4$) exhibiting the poorest performance. Upon returning to a current density of 12.8 mA g^{-1}, the discharge capacities were 161 mA h g^{-1} for pristine NVPF, 122 mA h g^{-1} for NVPF-Br ($x = 0.1$), 169 mA h g^{-1} for NVPF-Br ($x = 0.2$), 156 mA h g^{-1} for NVPF-Br ($x = 0.3$), and 121 mA h g^{-1} for NVPF-Br ($x = 0.4$). All cathodes displayed a slight capacity increase upon revision, which is attributed to improved electrode–electrolyte wetting.[42–45] Notably, NVPF-Br ($x = 0.2$) achieved the highest discharge capacity (169 mA h g^{-1}), corresponding to the insertion of 2.64Na$^+$ ions, and retained 154 mA h g^{-1} over 80 cycles at 25.6 mA g^{-1}. The refined XRD model reveals that structural rearrangement in NVPF-Br ($x = 0.2$) leads to an expansion of the 2D tunnel width, which facilitates enhanced Na-ion migration. Additionally, its superior capacity retention indicates the formation of a stable CEI layer on the surface, as evidenced by the F 1s XPS spectra after the initial cycle (Fig. 3b). Although pristine NVPF exhibits the initial highest capacity, it fails to maintain stability during rate-controlled cycling, indicating the presence of a less robust protective layer. The intercalation/deintercalation of more than 2Na$^+$ ions in NVPF leads to severe structural and morphological instability, as observed in our previous study.[20] Among the Br-substituted materials, NVPF-Br ($x = 0.4$) exhibits the lowest discharge capacity upon returning to a current density of 25.6 mA g^{-1} and shows gradual capacity deterioration with

increasing cycle number. This behavior further confirms the instability of the CEI layer, as anticipated by the F 1s XPS spectra (Fig. S3). To further evaluate the cycling stability of the materials, long-term cycling performance was assessed at a current density of 64 mA g^{-1}, as shown in Fig. 4b.

Pristine NVPF reaches its maximum capacity (150 mA h g^{-1}) after 45 cycles but undergoes rapid degradation, thereafter, retaining only 40% of its initial capacity (50.6 mA h g^{-1}) after 150 cycles. In contrast, NVPF-Br ($x = 0.2$) achieves a peak discharge capacity of 169 mA h g^{-1} once full wetting is established and retains 134 mA h g^{-1} even after 150 cycles, maintaining 100% coulombic efficiency (Fig. S3). This corresponds to a stable (de)intercalation process of 2.1Na$^+$ ions. Amongst the Br-substituted cathodes, NVPF-Br ($x = 0.1$) shows the lowest discharge capacity, indicating an unfavorable Na$^+$ (de)intercalation mechanism likely caused by the structural incompatibility arising from F replacement. According to the microstructural parameters obtained from structural refinement, the c lattice parameter in NVPF-Br ($x = 0.1$) decreases significantly, indicating structural instability. The V$_2$O$_8$F$_{2.7}$Br$_{0.3}$ bioctahedral unit appears to interfere with the orthorhombic distortion in the ab plane, which may hinder Na$^+$ ion interactions and contribute to early capacity fading. A similar trend is observed for the highest Br-substitution, NVPF-Br ($x = 0.4$), where rapid capacity fading confirms structural collapse during cycling. According to the refined XRD structure measurements, the generation of a large microstrain for NVPF-Br ($x = 0.4$) causes the contraction of the lattice parameters and decreases the unit cell volume, which may hinder Na$^+$ (de)intercalation. Additionally, the coulombic efficiency for both $x = 0.1$ and $x = 0.4$ remains below 100% (Fig. S3), further confirming the structural instability associated with the Na$^+$ insertion mechanism.

However, the microstructure of the cathode materials plays a key role in determining electrode wettability. This is reflected in the surface morphology of the synthesized microspheres, as shown in Fig. 1. The surface porosity is higher for NVPF and NVPF-Br ($x = 0.4$), which helps to attain the electrolyte saturation at an early stage. However, this also accelerates surface degradation, initiating a sharp capacity fading. In contrast, the smoother surface of NVPF-Br ($x = 0.2$) requires a longer time to obtain full wetting. However, the formation of a stable CEI layer effectively protects the surface from further degradation. In summary, an optimized amount of Br substitution in the NVPF structure is crucial to achieve high discharge capacity through extraction/insertion of more than two Na$^+$ ions, thereby achieving high discharge capacity along with improved stability. The ionic transport properties of NVPF and Br-substituted NVPF (NVPF-Br$_x$, $x = 0.1$, 0.2, 0.3, 0.4) were systematically investigated using the galvanostatic intermittent titration technique (GITT). The Na$^+$ diffusion coefficient (D_{Na^+}) was evaluated during the first charge–discharge cycle and compared across the synthesized cathode materials. For this measurement, a constant current pulse (8.5 mA g^{-1}) was applied for 10 minutes, followed by a relaxation period of 40 minutes. The sequence was repeated throughout the complete charge–discharge process. The corresponding time–voltage

profile from the GITT experiment is presented in Fig. 4c. The D_{Na^+} values were calculated using Fick's second law.[46] Fig. 4d and e illustrate the variation of D_{Na^+} during the charge and discharge processes, respectively. For pristine NVFP, the calculated D_{Na^+} is mainly within the range of 10^{-10} cm^2 s^{-1} (9.7 $\times 10^{-10}$ cm^2 s^{-1}). Upon Br substitution, it exhibits a significant increase, 1.1×10^{-9} cm^2 s^{-1} for $x = 0.1$, 2.1×10^{-9} cm^2 s^{-1} for $x = 0.2$, 1.4×10^{-9} cm^2 s^{-1} for $x = 0.3$ and 3.6×10^{-10} cm^2 s^{-1} for $x = 0.4$. Notably, the highest D_{Na^+} value is observed for NVPF-Br ($x = 0.2$), suggesting improved Na$^+$ transport kinetics. This improvement is likely due to structural modifications induced by the optimum level of Br substitution. During the discharge process, the D_{Na^+} value for NVPF-Br ($x = 0.2$) is enhanced to 3.76×10^{-9} cm^2 s^{-1}, the highest among the studied compositions. For comparison, the other D_{Na^+} values are NVPF (2.1×10^{-9} cm^2 s^{-1}), NVPF-Br ($x = 0.1$) (1.21×10^{-9} cm^2 s^{-1}), NVPF-Br ($x = 0.3$) (2.47×10^{-9} cm^2 s^{-1}), and NVPF-Br ($x = 0.4$) (8×10^{-10} cm^2 s^{-1}). These findings indicate that Br substitution at $x = 0.2$ effectively reduces the Na$^+$ diffusion path length, thereby facilitating ionic mobility within the host structure.[14,46,47]

To gain further insight into surface stability, a post-cycling high-resolution SEM (HRSEM) study was performed, as presented in Fig. 5a–e. The presence of cracks on the surface of pristine NVPF (magnified image at inset Fig. 5a) indicates the instability of the surface-protecting CEI layer during intercalation/deintercalation of more than 2Na$^+$ ions. This observation is consistent with the cycling performance. For NVPF-Br ($x = 0.1$), the rupture of the microsphere structure after

cycling establishes the incompatibility of the material with prolonged cycling and reflects the inadequacy of the surface protective layer in maintaining structural integrity. Similar surface breakage is observed for NVPF-Br ($x = 0.3$) and NVPF-Br ($x = 0.4$), providing clear evidence of the lack of stable CEI formation on the surface and supporting their inability to retain capacity during extended cycling. Interestingly, NVPF-Br ($x = 0.2$) displays the most stable post-cycled morphology, without any signs of surface cracking. It also suggests that side reactions are well-controlled and that the structural stability of the material is preserved. Moreover, the quality of the CEI layer is examined using post-cycling F 1s XPS spectra, represented in Fig. 6a, where the signature of the NaF peak is one of the major factors to describe the aspects of the formed CEI layer, as widely reported in the literature.[41] In accordance with our earlier
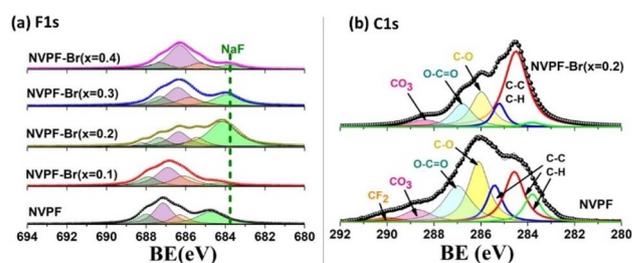

Fig. 6 Post-cycling surface chemical analysis of cathode materials. (a) F 1s XPS spectra of cathodes after cycling. (b) C 1s XPS spectra of post-cycled NVPF and NVPF-Br ($x = 0.2$).
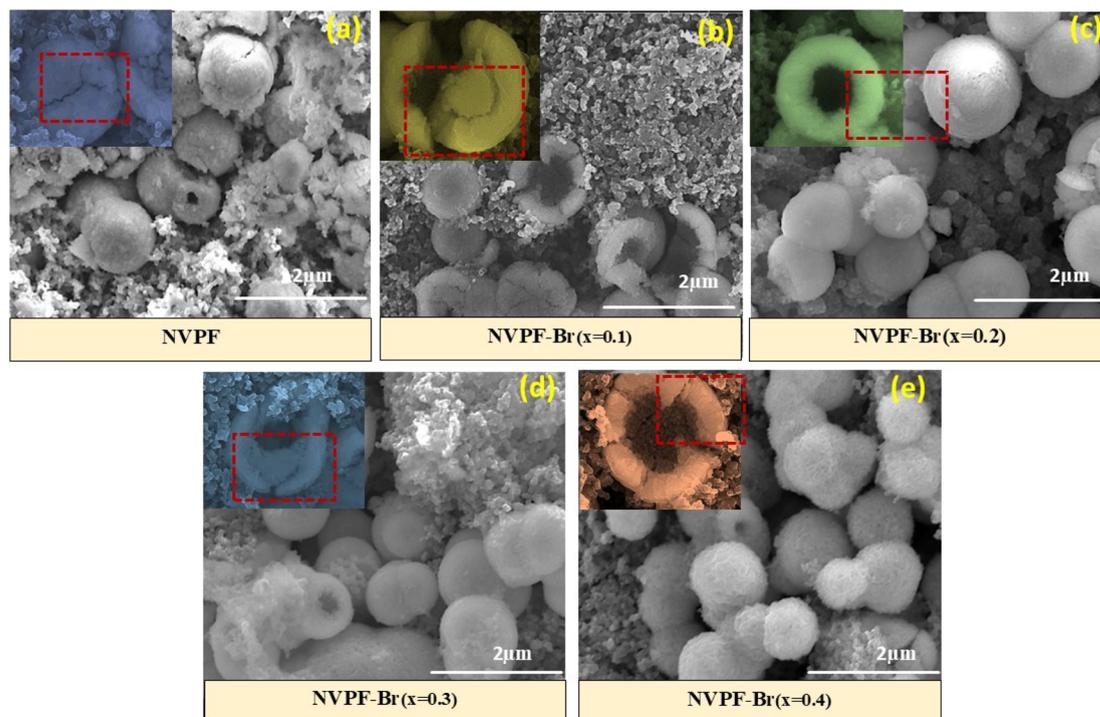

Fig. 5 Post-cycling SEM image of cathode surfaces. Surface morphologies of cathodes after cycling for pristine NVPF and Br-substituted samples: (a) NVPF, (b) NVPF-Br ($x = 0.1$), (c) NVPF-Br ($x = 0.2$), (d) NVPF-Br ($x = 0.3$), and (e) NVPF-Br ($x = 0.4$) [magnification 45 000×, scale bar indicates 2 µm length]. Insets show corresponding high-magnification images of the surface features [magnification 115 000×].

33300 | *J. Mater. Chem. A*, 2025, **13**, 33294–33304

This journal is © The Royal Society of Chemistry 2025

discussion (Fig. 3b), the intense NaF peak (~684–685 eV) in the F 1s spectra signifies the potency of the CEI layer. Consequently, the relative intensity of the NaF peak for the cycled NVPF-Br (x = 0.2) electrode is the highest among all samples, indicating a strong surface protective layer. This observation is supported by the HRSEM results and the long-term cycle cell performance. Furthermore, the complete breakage of the microsphere in the case of NVPF-Br (x = 0.1 and x = 0.4), as observed from the HRSEM (Fig. 5b and e), is well supported by the minimal trace of NaF peak in the F 1s spectra, as shown in Fig. 6a. For NVPF and NVPF-Br (x = 0.3), the insufficient intensity of the NaF peak in the F 1s spectra indicates the inadequacy of the protective CEI layer, which is also reflected in their HRSEM image (Fig. 5a and d). Additionally, the C 1s spectra of the post-cycled NVPF and NVPF-Br (x = 0.2) cathodes are shown in Fig. 6b, where the C–C/C=C bond from conductive carbon and C–H bond from hydrocarbon are located at 284.6 eV and 285.8 eV, respectively.[36–38] The peaks located at 286.2 eV, 287 eV, and 288.8 eV are assigned to C–O, O–C=O, and CO_3, respectively, originating from (R–C*–OC–O(O)) and (CO_3^{2-}, R–C–OC*O (O)) groups, indicating the presence of carbonate components in the CEI layer.[32,41] However, the area under these curves is higher for pristine NVPF compared to the NVPF-Br (x = 0.2), further indicating reduced carbonate formation on the NVPF-Br (x = 0.2) cathode surface. This reduced carbonate content justifies the excellent capacity retention of NVPF-Br (x = 0.2) even within the extended potential regime. Furthermore, the trace of the CF_2 bond (at 290 eV) in the post-cycled NVPF cathode, originating from the PVDF binder, confirms the presence of a thinner CEI layer, which contributes to the material's instability over long-term cycling.[41]

The post-cycled structural shift of the electrodes was recorded and is shown in Fig. 7a–e. No extra peaks are observed for any of the materials after cycling, indicating the preservation of their phase structure without the formation of impurities. However, the magnified 2θ region of NVPF, NVPF-Br (x = 0.1), and NVPF-Br (x = 0.3) shows peak shifts towards lower angles, revealing an increase in interplanar spacings after prolonging Na^+ (de)intercalation process. In contrast, the enlarged view of NVPF-Br (x = 0.4) displays peak shifts toward higher 2θ values, indicating a contraction of interlayer spacing within the structure, which could reasonably explain the observed capacity fading. Notably, for NVPF-Br (x = 0.2), no peak shifting is observed (inset of Fig. 7c), further confirming its structural stability after a reversible insertion/de-insertion process along with the highest capacity retention.

First-principles calculation

The role of Br in optimizing the capacity and cycling stability of $Na_3V_2(PO_4)_2F_3$ led us to perform first-principles calculations to better understand its thermodynamic and kinetic properties of Na ion. For computational convenience, here we focused on the analog $Na_3V_2(PO_4)_2F_2Br$, which closely represents the experimentally synthesized NVPF-Br (x = 0.2). From the Rietveld refinement of the X-ray diffraction pattern of the experimentally synthesized $Na_3V_2(PO_4)_2F_2Br$, it was found that the Br replaces
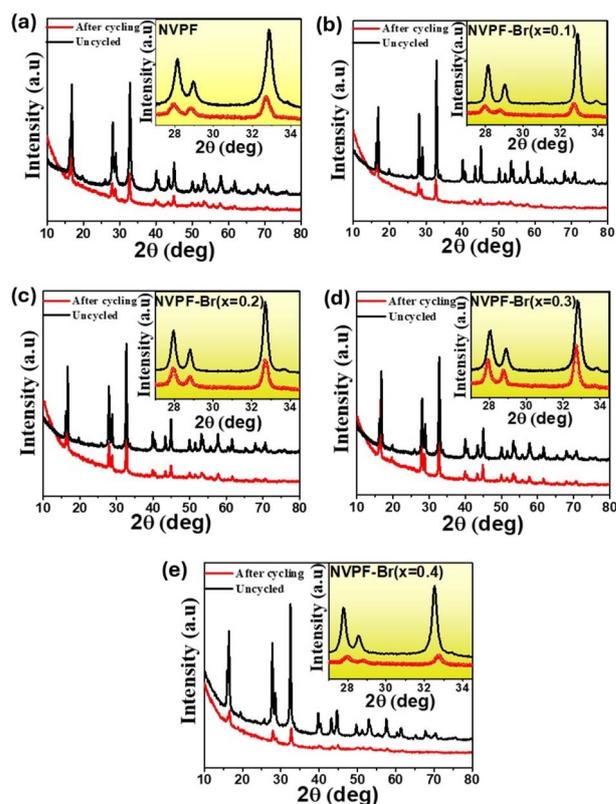

Fig. 7 Post-cycling XRD spectra of cathodes. (a) NVPF, (b) NVPF-Br (x = 0.1), (c) NVPF-Br (x = 0.2), (d) NVPF-Br (x = 0.3), and (e) NVPF-Br (x = 0.4). Insets show the magnified 2θ region.

~20% of the F sites within the structure. The configuration was further optimized using DFT calculations, as shown in Fig. 8a. The structural optimization yields a $V_2O_8F_2Br$ bioctahedral unit within $Na_3V_2(PO_4)_2F_2Br$ (Fig. 8b), which is corner-shared with PO_4 tetrahedra. The bioctahedral unit is a typical recurrent structural motif in the fully fluorinated $Na_xV_2(PO_4)_2F_3$ framework.[49,50] As shown in Fig. 8b, Na ions in $Na_3V_2(PO_4)_2F_2Br$ structure are populated within a prismatic polyhedron consisting of four O atoms, two F atoms, and one Br atom. The positions of three systematically distinct Na sites, analogous to those in the $Na_xV_2(PO_4)_2F_3$ framework,[49–51] are superimposed in Fig. 8c. In our nomenclature, the Na1 sites are aligned such that the connection of F–Na1 is along [010], Na2 sites are aligned parallel to [100], and the Na3 sites along [110] are interstitial sites and bridge the Na1 and Na2 sites. Our computational results identified two thermodynamically stable occupied Na sites in the synthesized $Na_3V_2(PO_4)_2F_2Br$ material, i.e., Na1 and Na2, with occupancies of approximately 2× Na1 and 1× Na2 per formula unit (Fig. 8a). Additionally, V was predicted to exhibit a +3 oxidation state.

To gain insights into Na-ion transport kinetics within the synthesized $Na_3V_2(PO_4)_2F_2Br$ material, we performed nudged elastic band (NEB) calculations. Two representative 2-dimensional (2D) migration pathways were selected (Fig. 8d).[48] Fig. 8e illustrates the intra-unit pathway, represented by blue-ring arrows, while Fig. 8f shows the inter-unit pathway,
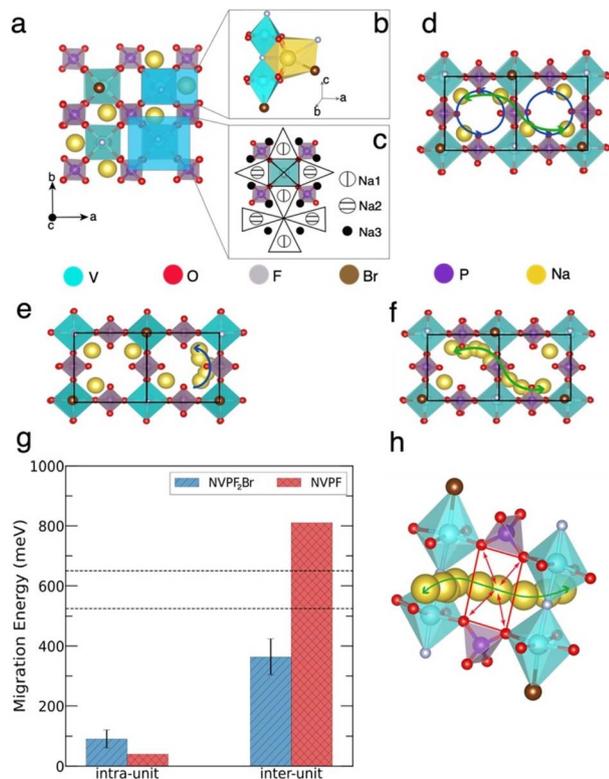
This journal is © The Royal Society of Chemistry 2025

J. Mater. Chem. A, 2025, **13**, 33294–33304 | **33301**

Fig. 8 Na-ion kinetic behaviors for the synthesized $Na_3V_2(PO_4)_2F_2Br$ structure. (a) Structural topology of the *ab*-plane view of the $Na_3V_2(PO_4)_2F_2Br$ at the level of GGA+U theory. The structure crystallizes in the monoclinic structure ($P2_1/c$ space group). (b) $V_2O_8F_2Br$ bi-octahedral unit (cyan polyhedra), with atoms color-coded as follows: V (cyan), O (red), F (silver), Br (brown), P (purple), and Na (yellow). (c) Schematic representation of the Na1, Na2, and Na3 sites corresponding to the 3 typical Na sites in the $Na_xV_2(PO_4)_2F_3$ structure. (d) Illustration of two Na-ion migration pathways: intra-unit (blue-ring arrows) and inter-unit (green arrows). Computed migration pathways for (e) intra-unit and (f) inter-unit. (g) Comparison of the calculated migration energies for intra-unit and inter-unit pathways in $Na_3V_2(PO_4)_2F_2Br$ (NVPF₂Br) and $Na_3V_2(PO_4)_2F_3$ (NVPF). Data for NVPF are taken from ref. 26 and48. Error bars ($\sim\pm50$ meV) are indicated, and dashed black lines mark the typical migration barrier energy ($\sim$525–650 meV). (h) Local diffusion coordinate of the Na-ion migrating through the inter-unit pathway (from panel (f)). The red rectangle shows the bottleneck around the saddle point. The red arrows specify the Na–O bond length, and the green arrows denote the diffusion pathway.

represented by a green arrow. The intra-unit pathway captures the Na$^+$ migration between the Na1 and Na2 sites *via* the interstitial Na3 site. In contrast, the inter-unit pathway describes Na$^+$ migration across the intra-unit rings, contributing to the macroscopic diffusion within the $Na_3V_2(PO_4)_2F_2Br$ structure. As shown in Fig. 8g, our computations reveal that the migration activation energy for the intra-unit pathway in $Na_3V_2(PO_4)_2F_2Br$ is $\sim$91 meV, while a higher barrier of $\sim$364 meV is required for inter-unit migration. This indicates that the inter-unit pathway behaves as the rate-limiting step for the migration of Na$^+$ ions with the $Na_3V_2(PO_4)_2F_2Br$ structure. For comparison, the migration energy for fast ions, *i.e.*, Li$^+$ or Na$^+$, is typically estimated to be $\sim$525 meV in micro-sized particles, and

$\sim$650 meV in nano-particles.[52,53] Therefore, the computed migration energies for both pathways in $Na_3V_2(PO_4)_2F_2Br$ are below the tolerance thresholds, suggesting feasible Na-ion migration and sustainable discharge/charge rate within the synthesized $Na_3V_2(PO_4)_2F_2Br$. The fully fluorinated analog, $Na_3V_2(PO_4)_2F_3$, has been reported to show a comparable migration energy of $\sim$40 meV for the intra-unit pathway.[48] At the same time, the barrier energy for inter-unit migration within $Na_3V_2(PO_4)_2F_3$ is computationally evaluated to be $\sim$811 meV, which is $\sim$25% higher than that of $Na_3V_2(PO_4)_2F_2Br$.[26,48] In comparison, the Br-substituted $Na_3V_2(PO_4)_2F_2Br$ exhibits significantly improved diffusion kinetics.

There are several factors that account for the optimized ion transport kinetics in $Na_3V_2(PO_4)_2F_2Br$ over $Na_3V_2(PO_4)_2F_3$. First, our computations revealed that the volume of $Na_3V_2(PO_4)_2F_2Br$ is about 244.09 Å^3 f.u.$^{-1}$ (formula unit), which is approximately 6.9% larger than that of $Na_3V_2(PO_4)_2F_3$ ($\sim$228.37 Å^3 f.u.$^{-1}$). This cell expansion, resulting from the replacement of $\sim$20% of F$^-$ with the larger Br$^-$ (ionic radius of $\sim$1.96 Å), could give rise to the less-hindered migration pathways within the structure. Second, as represented in Fig. 8h, Na$^+$ macroscopically migrates through the inter-unit pathway that proceeds through a rectangular "bottleneck" formed by 4O atoms from two adjacent PO$_4$ tetrahedra positioned on either side of the pathway. This structural feature constrains the migration channel. The average Na–O bond length between the Na$^+$ ion at the saddle point and the 4 surrounding O atoms is $\sim$2.39 Å in $Na_3V_2(PO_4)_2F_2Br$, which is larger than the corresponding value in $Na_3V_2(PO_4)_2F_3$ ($\sim$2.15 Å).[50] This indicates that the "bottleneck" face area is roughly 15% larger in $Na_3V_2(PO_4)_2F_2Br$. Therefore, the electrostatic repulsion from the nearby cations to the migrating Na$^+$ ion around the saddle point (corresponding to the maximum in migration energy) is reduced. This contributes to the lower energy of the activated state and thus facilitates more efficient ion migration along the rate-limiting inter-unit pathway within $Na_3V_2(PO_4)_2F_2Br$. Third, the strong Na-vacancy orderings in the $Na_3V_2(PO_4)_2F_3$ could be disrupted by the additional configurational entropy introduced by the mixing of F and Br. This entropy-driven effect can further facilitate Na$^+$ ion migration in $Na_3V_2(PO_4)_2F_2Br$.[26,27,48,54] These results suggest that Na-ion diffusion kinetics are optimized in the Br-substituted $Na_3V_2(PO_4)_2F_2Br$ compound (and related NVPF-Br ($x = 0.2$) analogs), enabling improved cycling performance of the as-synthesized NVPF-Br ($x = 0.2$) cathode materials.

Conclusions

We propose a strategy to activate the third Na$^+$ ion in the NVPF cathode, thereby enhancing the energy density of sodium-ion storage. A series of Br-substituted NVPF-Br cathodes ($x = 0.1$, 0.2, 0.3, and 0.4) were synthesized *via* a solvothermal process, where partial replacement of F$^-$ with Br$^-$ expands the Na-ion accommodation layer without altering the V^{3+} oxidation state, as confirmed by XPS. Structural and morphological analyses (XRD, HRSEM, and HRTEM) reveal a hollow spherical morphology with a stable crystalline phase. Rietveld refinement

33302 | *J. Mater. Chem. A*, 2025, **13**, 33294–33304

This journal is © The Royal Society of Chemistry 2025

supports a strong correlation between microstructural parameters and electrochemical performance.

Among all compositions, NVPF-Br ($x = 0.2$) exhibits the highest discharge capacity (169 mA h g^{-1} at 64 mA g^{-1}) within 1.2–4.3 V and retains 134 mA h g^{-1} after 150 cycles with 100% coulombic efficiency, indicating the successful (de)intercalation of more than 2Na$^+$ ions. Post-cycling surface analysis confirms a crack-free morphology, while XPS reveals a higher NaF content in the CEI layer, contributing to improved cycling stability and reduced carbonate formation. Structural refinement and DFT calculations further validate that Br substitution at $x = 0.2$ increases the 2D tunnel width and unit cell volume, promoting reversible Na-ion (de)intercalation. Additionally, the lower electronegativity of Br reduces migration activation energy, enhancing Na-ion transport kinetics.

This study presents a novel approach to improving the capacity and cycling stability of NVPF cathodes through optimized crystal design, offering a promising solution to long-standing challenges in sodium-ion battery development.

Author contributions

Sankalpita Chakrabarty: conceptualization, methodology, formal analysis, validation, writing – original draft; Ziliang Wang: computational analysis and writing; Arun Krishnan: resources; Arad Paperni: resources; Sarah Taragin: resources; Reut Yemini: resources; Ilana Perelshtein: instrumental facility; Ayan Mukherjee: conceptualization, validation, investigation, writing – review & editing; Malachi Noked: supervision, writing – review & editing.

Conflicts of interest

There are no conflicts to declare.

Data availability

The data that support the findings of this study are available from the corresponding authors upon reasonable request.

Supplementary information include the experimental part, fitted XRD graphs, structural refinement parameters, variation of coulombic efficiency with cycling and computational methodology. See DOI: https://doi.org/10.1039/d5ta05400a.

Acknowledgements

References

1 H. Wu, T. Wen, Y. Ding, R. Huang, Y. Zeng, X. Pu and Z. Chen, *Batteries Supercaps*, 2024, **16**, 2–10.

2 N. Feature, *Nature*, 2014, **507**, 26–28.

3 K. N. Wood, M. Noked and N. P. Dasgupta, *ACS Energy Lett.*, 2017, **2**, 664–672.

4 B. Xu, D. Qian, Z. Wang and Y. S. Meng, *Mater. Sci. Eng., R*, 2012, **73**, 51–65.

5 I. Hasa, S. Mariyappan, D. Saurel, P. Adelhelm, A. Y. Koposov, C. Masquelier, L. Croguennec and M. Casas-Cabanas, *J. Power Sources*, 2021, **482**, 228872.

6 X. Ma, X. Cao, Y. Zhou, S. Guo, X. Shi, G. Fang, A. Pan, B. Lu, J. Zhou and S. Liang, *Nano Res.*, 2020, **13**, 3330–3337.

7 R. Fang, J. Olchowka, C. Pablos, R. Bianchini Nuernberg, L. Croguennec and S. Cassaignon, *ACS Appl. Energy Mater.*, 2022, **5**, 1065–1075.

8 H. Xu, Q. Yan, W. Yao, C.-S. Lee and Y. Tang, *Small Struct.*, 2022, **3**, 2100217.

9 B. Singh, Z. Wang, S. Park, G. S. Gautam, J. N. Chotard, L. Croguennec, D. Carlier, A. K. Cheetham, C. Masquelier and P. Canepa, *J. Mater. Chem. A*, 2021, **9**, 281–292.

10 A. Kamiyama, K. Kubota, D. Igarashi, Y. Youn, Y. Tateyama, H. Ando, K. Gotoh and S. Komaba, *Angew. Chem., Int. Ed.*, 2021, **60**, 5114–5120.

11 A. Mukherjee, S. Chakrabarty, S. Taragin, E. Evinstein, P. Bhanja, A. Joshi, H. Aviv, I. Perelshtein, M. Mohapatra, S. Basu and M. Noked, *Small*, 2024, 2308886.

12 K. Wang, H. Zhuo, J. Wang, F. Poon, X. Sun and B. Xiao, *Adv. Funct. Mater.*, 2023, **33**, 2212607.

13 J. Mu, T. Cai, W. Dong, C. Zhou, Z. Han and F. Huang, *Chem. Eng. J.*, 2023, **471**, 144403.

14 M. Wang, Y. Wang, Y. Xin, Q. Liu, F. Wu and H. Gao, *ACS Appl. Energy Mater.*, 2023, **6**, 4453–4461.

15 S. Chakrabarty, T. Sharabani, S. Taragin, R. Yemini, A. Maddegalla, I. Perelshtein, A. Mukherjee and M. Noked, *J. Energy Storage*, 2024, **84**(1–12), 111507.

16 C. Sun, L. L. Zhang, X. Q. Xiong, Z. R. Deng, H. Bin Sun and X. L. Yang, *ACS Sustain. Chem. Eng.*, 2024, **12**, 10892–10904.

17 C. Xu, Q. Fu, W. Hua, Z. Chen, Q. Zhang, Y. Bai, C. Yang, J. Zhao and Y. S. Hu, *ACS Nano*, 2024, **18**, 18758–18768.

18 Y. F. Liu, K. Han, D. N. Peng, L. Y. Kong, Y. Su, H. W. Li, H. Y. Hu, J. Y. Li, H. R. Wang, Z. Q. Fu, Q. Ma, Y. F. Zhu, R. R. Tang, S. L. Chou, Y. Xiao and X. W. Wu, *InfoMat*, 2023, **5**, 1–43.

19 H. Yang, Q. Zhang, M. Chen, Y. Yang and J. Zhao, *Adv. Funct. Mater.*, 2024, **34**, 1–9.

20 A. Mukherjee, T. Sharabani, I. Perelshtein and M. Noked, *Batteries Supercaps*, 2020, **3**(1), 52–55.

21 J. Olchowka, L. H. B. Nguyen, E. Petit, P. S. Camacho, C. Masquelier, D. Carlier and L. Croguennec, *Inorg. Chem.*, 2020, **59**, 17282–17290.

22 T. Broux, T. Bamine, F. Fauth, L. Simonelli, W. Olszewski, C. Marini, M. Ménétrier, D. Carlier, C. Masquelier and L. Croguennec, *Chem. Mater.*, 2016, **28**, 7683–7692.

23 B. Zhang, R. Dugas, G. Rousse, P. Rozier, A. M. Abakumov and J. M. Tarascon, *Nat. Commun.*, 2016, **7**, 1–9.

24 M. Bianchini, P. Xiao, Y. Wang and G. Ceder, *Adv. Energy Mater.*, 2017, **7**, 1–8.

25 Y. U. Park, D. H. Seo, H. Kim, J. Kim, S. Lee, B. Kim and K. Kang, *Adv. Funct. Mater.*, 2014, **24**, 4603–4614.

This journal is © The Royal Society of Chemistry 2025

J. Mater. Chem. A, 2025, **13**, 33294–33304 | **33303**

26 S. T. Dacek, W. D. Richards, D. A. Kitchaev and G. Ceder, *Chem. Mater.*, 2016, **28**, 5450–5460.

27 S. C. C. van der Lubbe, Z. Wang, D. K. J. Lee and P. Canepa, *Chem. Mater.*, 2023, **35**, 5116–5126.

28 G. Yan, S. Mariyappan, G. Rousse, Q. Jacquet, M. Deschamps, R. David, B. Mirvaux, J. W. Freeland and J. M. Tarascon, *Nat. Commun.*, 2019, **10**, 585.

29 M. Xu, P. Xiao, S. Stauffer, J. Song, G. Henkelman and J. B. Goodenough, *Chem. Mater.*, 2014, **26**, 3089–3097.

30 Y. Zhang, S. Guo and H. Xu, *J. Mater. Chem. A*, 2018, **6**, 4525–4534.

31 A. Mukherjee, T. Sharabani, R. Sharma, S. Okashy and M. Noked, *Batteries Supercaps*, 2020, **3**, 510–518.

32 T. Sharabani, S. Taragin, I. Perelshtein, M. Noked and A. Mukherjee, *Small*, 2021, **17**, 1–9.

33 G. Yan, S. Mariyappan, G. Rousse, Q. Jacquet, M. Deschamps, R. David, B. Mirvaux, J. W. Freeland and J. M. Tarascon, *Nat. Commun.*, 2019, **10**, 1–12.

34 P. Wang, B. Huang, Q. Zhang, X. Zhang, X. Qin, Y. Dai, J. Zhan, J. Yu, H. Liu and Z. Lou, *Chem.–Eur. J.*, 2010, **16**, 10042–10047.

35 J. Xu, Q. Zhang and Y.-T. Cheng, *J. Electrochem. Soc.*, 2016, **163**, A401–A405.

36 R. Tatara, P. Karayaylali, Y. Yu, Y. Zhang, L. Giordano, F. Maglia, R. Jung, J. P. Schmidt, I. Lund and Y. Shao-Horn, *J. Electrochem. Soc.*, 2019, **166**, A5090–A5098.

37 S. Han, Y. Liu, H. Zhang, C. Fan, W. Fan, L. Yu and X. Du, *Surf. Interface Anal.*, 2020, **52**, 364–373.

38 Z. Lu, J. Yu, J. Wu, M. B. Effat, S. C. T. Kwok, Y. Lyu, M. M. F. Yuen and F. Ciucci, *Energy Storage Mater.*, 2019, **18**, 311–319.

39 Y. Wu, X. Liu, L. Wang, X. Feng, D. Ren, Y. Li, X. Rui, Y. Wang, X. Han, G. L. Xu, H. Wang, L. Lu, X. He, K. Amine and M. Ouyang, *Energy Storage Mater.*, 2021, **37**, 77–86.

40 M. I. Nandasiri, L. E. Camacho-Forero, A. M. Schwarz, V. Shutthanandan, S. Thevuthasan, P. B. Balbuena, K. T. Mueller and V. Murugesan, *Chem. Mater.*, 2017, **29**, 4728–4737.

41 J. Fondard, E. Irisarri, C. Courrèges, M. R. Palacin, A. Ponrouch and R. Dedryvère, *J. Electrochem. Soc.*, 2020, **167**, 070526.

42 J. Scholz, B. Kayaalp, A. C. Juhl, D. Clemens, M. Fröba and S. Mascotto, *ACS Energy Lett.*, 2018, **3**, 387–392.

43 D. H. Jeon, *Appl. Mater. Today*, 2021, **22**, 100976.

44 L. Li, C. Wei and P. Shen, *J. Eur. Ceram. Soc.*, 2020, **40**, 4281–4289.

45 M. Lautenschlaeger, B. Prifling, B. Kellers, J. Weinmiller, T. Danner, V. Schmidt and A. Latz, *Batteries Supercaps*, 2022, e202200090.

46 W. G. Morais, E. C. Melo and R. M. Torresi, *Mater. Adv.*, 2024, **5**, 5070–5079.

47 K. Lin, Q. Liu, Y. Zhou, H. Chen, J. Liu, J. Z. Zhao and X. Hou, *Chem. Eng. J.*, 2023, **463**, 142464.

48 I. L. Matts, S. Dacek, T. K. Pietrzak, R. Malik and G. Ceder, *Chem. Mater.*, 2015, **27**, 6008–6015.

49 M. Bianchini, N. Brisset, F. Fauth, F. Weill, E. Elkaim, E. Suard, C. Masquelier and L. Croguennec, *Chem. Mater.*, 2014, **26**, 4238–4247.

50 M. Bianchini, F. Fauth, N. Brisset, F. Weill, E. Suard, C. Masquelier and L. Croguennec, *Chem. Mater.*, 2015, **27**, 3009–3020.

51 L. H. B. Nguyen, A. Iadecola, S. Belin, J. Olchowka, C. Masquelier, D. Carlier and L. Croguennec, *J. Phys. Chem. C*, 2020, **124**, 23511–23522.

52 T. Chen, G. Sai Gautam and P. Canepa, *Chem. Mater.*, 2019, **31**, 8087–8099.

53 Z. Rong, R. Malik, P. Canepa, G. Sai Gautam, M. Liu, A. Jain, K. Persson and G. Ceder, *Chem. Mater.*, 2015, **27**, 6016–6021.

54 Z.-Y. Gu, J.-Z. Guo, J.-M. Cao, X.-T. Wang, X.-X. Zhao, X.-Y. Zheng, W.-H. Li, Z.-H. Sun, H.-J. Liang and X.-L. Wu, *Adv. Mater.*, 2022, **34**, 2110108.

33304 | *J. Mater. Chem. A*, 2025, **13**, 33294–33304

This journal is © The Royal Society of Chemistry 2025